nature communications

Article

https://doi.org/10.1038/s41467-025-59771-6

Post-oxidation of all-organic electrocatalysts to promote O—O coupling in water oxidation

Received: 1 October 2024

Accepted: 30 April 2025

Published online: 12 May 2025

Check for updates

Chun-Ting He[1,5] ✉, Li-Hong Yu[1,5], Haiming Liu[2,5], Qing Wang[2], Zi-Ming Ye[3], Jia Zhang[1] ✉, Li-Dong Wang[1], Mei-Qian He[1], Xue-Feng Zhang[1], Hong-Gang Du[1], Zi-Wei Lu[1], Jian Yang[1], Hai-Hua Huang[1] & Xiao-Ming Chen[4]

Covalently bonded metal-free electrocatalysts exhibit significant potential for sustainable energy technologies, yet their performances remain unsatisfactory compared with metal-based catalysts. Herein, we propose an all-organic electrocatalyst, MEC-2, that conforms to the infrequent oxide path mechanism in alkaline oxygen evolution reaction through post-oxidation modification. MEC-2 achieves an intrinsic overpotential of 257.7 ± 0.6 mV at 10 mA·cm^{-2} and possesses durability with negligible degradation over 100,000 CV cycles or 250 h of operation at 1.0 A·cm^{-2}, being comparable to the advanced metal-based OER electrocatalysts. The ^{18}O-labeled operando characterization and theoretical calculations unveil that post-oxidation modification enhances the electron affinity to OH intermediates, and adjusts the adsorption configuration and proximity distance of O intermediates, thereby promoting direct O–O radical coupling. In this work, we show a fresh perspective for understanding the role of non-metallic elements/functional groups in electrocatalysis, and to a certain extent, narrows the gap between all-organic electrocatalysts and metal-based electrocatalysts.

With the advancement of energy conversion technologies, such as sustainable water electrolysis, rechargeable energy storing devices, and carbon reduction systems, the oxygen evolution reaction (OER) has emerged as a significant hurdle in their industrialization due to its involvement in multi-electron transfer pathways and low efficiency[1–4]. Consequently, the development of an ideal electrocatalyst for OER should possess the ability to dissociate water molecules under the appropriate applied voltage, and exhibit good stability under highly chemical corrosion conditions[5,6]. Up to date, the dominant OER electrocatalysts remain metal-based materials due to the rich and varied *d* electrons in transition-metal atoms[7–9]. In contrast, metal-free materials, characterized by their *p* valence orbitals, usually exhibit unsatisfactory performance in electrocatalytic oxygen evolution. Nevertheless, such materials connected by robust covalent bonds offer unique advantages in catalysis, including environmental friendliness, abundant availability, cost-effectiveness, and strong tolerance to diverse acid and alkali environments[10,11]. In recent years, carbon-based metal-free materials, including heteroatom-doped porous carbon, graphene-carbon nanotube composites, carbon nitrides, and organogel, have demonstrated significant potential as efficient electrocatalysts[12–15]. However, the precise modification of inorganic carbons or disordered polymers is challenging, making it difficult to predict their active structures and investigate reaction mechanisms, which hinders their further development[16,17]. Covalent organic frameworks (COFs) are an emerging class of porous organic polymers covalently linked by well-defined building units, which allow for rational control over their structural motifs[18–20]. COFs exhibit high specific surface areas, adjustable pore sizes, notable stability, and structurally tunable with atomic

[1]Key Lab of Fluorine and Silicon for Energy Materials and Chemistry of Ministry of Education, College of Chemistry and Materials, Jiangxi Normal University, Nanchang 330022, China. [2]School of Physical Science and Technology, ShanghaiTech University, Shanghai 201210, China. [3]Fujian Key Laboratory of Polymer Materials, College of Chemistry and Materials Science, Fujian Normal University, FuZhou 350007, China. [4]MOE Key Laboratory of Bioinorganic and Synthetic Chemistry, School of Chemistry, Sun Yat-Sen University, Guangzhou 510275, China. [5]These authors contributed equally: Chun-Ting He, Li-Hong Yu, Haiming Liu. ✉e-mail: hct@jxnu.edu.cn; zhangjia727@jxnu.edu.cn

precision[21–24]. These features make them highly promising for designing metal-free catalysts and advancing catalytic enhancement mechanisms by organic molecules. For instance, some well-designed COFs containing specific molecular motifs, such as the thienothiophene-pyrene TAPTt-COF (CC-3)[25], phenazine-linked COF-C_4N[26], thiadiazole-based C4-SHz COF[27], and imidazolium-based JUC-627-NS@G-2[28], have been verified to possess significant OER intrinsic activities, which show overpotentials of 389, 349, 320 and 275 mV on glassy carbon electrodes (GCEs) to achieve a current density of 10 mA·cm^{-2}, respectively.

The adsorbate evolution mechanism (AEM) and the lattice oxygen oxidation mechanism (LOM) are two widely accepted mechanisms for OER[29–31]. AEM involves multiple reaction intermediates such as OH*, O*, and OOH*, and are usually difficult in breaking the inherent linear scaling relationship between the adsorption energies of these intermediates, which seriously limits the substantial modulation of catalytic energy barriers both on metal-based and metal-free catalysts[32]. On the other hand, LOM involves the participation of activated lattice oxygen during OER, which facilitates O−O coupling and reduces the energy barriers[33,34]. However, the generation of oxygen vacancy defects in LOM easily leads to the dissolution of metal species into the electrolyte, resulting in rapid degradation of electrocatalysts[35,36]. Moreover, it is worth noting that it is extremely difficult to produce lattice oxygen in metal-free catalysts due to the firmness of covalent bonding. In comparison to AEM and LOM, the oxide path mechanism (OPM) provides an alternative approach to balancing activity and stability in OER[37], since it allows for direct O−O radical coupling without the involvement of lattice oxygen, thus avoiding the generation of oxygen vacancy defects that could compromise catalyst stability[38–40]. Besides, OPM eliminates the necessity for OOH* intermediates, which facilitates non-proportional regulation of the energy barriers at the elementary reaction steps. However, it is important to note that OPM requires active sites with appropriate atomic distances and electron affinities to promote the coupling of adjacent oxygen radicals. Unfortunately, as of now, there have been no reports of OPM occurring in all-organic materials.

Here, we show an all-organic electrocatalyst O-LZU-190@CNT (MEC-2, MEC: lab of molecule-based energy chemistry) through post-oxidation of a benzoxazole-based COF coated onto carbon nanotube (CNT), resulting in efficient catalysis of OER by following an infrequent OPM mechanism. By performing a facile oxidation, hydroxyl groups can be introduced into the periodically arranged benzoxazole units without damaging the COF backbone. The introduction of additional oxygen functional groups causes a shift in the adsorption position of O* on the carbon skeleton, resulting in a shorter adjacent oxygen distance of 2.615 Å for facilitating the O−O radical coupling. O-LZU-190@CNT delivers a low overpotential of 257.7 ± 0.6 mV at 10 mA·cm^{-2} and a small Tafel slope of 26.3 ± 0.7 mV·dec^{-1}. Moreover, the catalyst could operate continuously for over 250 h with a fluctuation of 1.7 mV at an ampere-level current density. A variety of *operando*/*non-operando* characterization techniques and theoretical calculations reveal distinctive alterations in the reaction intermediates and surface chemistry of the catalyst before and after post-oxidation modification, indicating a shift from AEM to OPM along with a reduced energy barrier in OER.

Results and discussion

Characterization of Catalysts

A post-oxidation modified metal-free COF, denoted as O-LZU-190, was synthesized from a benzoxazole-based LZU-190[41] through a facile low-temperature oxidation process in an air atmosphere. Additionally, considering the inherently low conductivity of COF, it was coated onto carbon nanotubes (CNTs) to enhance electron transport, resulting in O-LZU-190@CNT (Fig. 1a). Powder X-ray diffraction (PXRD) patterns of O-LZU-190(@CNT) are almost consistent with those of LZU-190(@CNT), respectively (Supplementary Fig. 1). Thermogravimetric analysis (TGA) confirmed the notable thermal stability of LZU-190 either in N_2 or air (Supplementary Fig. 3). Consequently, LZU-190 maintains its initial periodic structure without degradation by low-temperature oxidation. In addition, O-LZU-190 preserves the original nanosheet structure of LZU-190 with a thickness of ca. 1.5 nm (Fig. 1b and Supplementary Figs. 4–5). The high-resolution transmission electron microscope (HRTEM) images reveal that legible lattice fringes can be observed in both LZU-190 and O-LZU-190, corresponding to the (001) or (220) crystallographic facets (Fig. 1c and Supplementary Fig. 6a). Notably, the coating of catalysts on CNTs exhibits a thickness of ca. 0.83 nm, equivalent to 2 ~ 3 layers of the two-dimensional (2D) COF, ensuring good conductivity and effectively exposure of the active sites (Fig. 1d and Supplementary Fig. 6b). The incorporation of oxygen groups has improved the surface wettability of O-LZU-190, resulting in a contact angle reduction to 31.1° in comparison with LZU-190 (Fig. 1e). Analysis of the nitrogen sorption isotherms reveals that both LZU-190 and O-LZU-190 exhibit Type I adsorption behavior, characteristic of microporous materials (Supplementary Fig. 7). The pore size distributions further confirm that micropores predominantly contribute to the total pore volume of the COFs. O-LZU-190 exhibits a larger BET specific surface area of 396.8 m^2·g^{-1} compared with LZU-190 (328.4 m^2·g^{-1}), which could be attributed to the reduction of oligomers. This hypothesis is also supported by the slight increase in mesopore volume observed in O-LZU-190, being consistent with the liberation of pore space following oxidative treatment. Additionally, elemental mappings derived from energy dispersive X-ray spectrometry (EDS) demonstrated uniform distributions of C, N, and O elements throughout the samples (Fig. 1f).

To gain insight into the structural impact of post-oxidation on LZU-190(@CNT), we prepared LZU-191(@CNT) and BO-COF[42](@CNT) as control samples. The corresponding oxidized versions of these materials were denoted as O-LZU-191(@CNT) and O-BO-COF(@CNT), respectively. Notably, LZU-191 features larger pore size than LZU-190, which translates to fewer benzoxazole sites per unit area available for oxidation. On the other hand, BO-COF lacks any potential oxidation sites (Fig. 2a). Comprehensive PXRD, SEM and TEM analyzes demonstrated that both O-LZU-191 and O-BO-COF retained their original structural integrities and morphologies after the post-oxidation modification (Supplementary Figs. 8-13). Elemental analyzes revealed a notable increase in oxygen content for both LZU-190 and LZU-191 after oxidation. Conversely, the oxygen content in BO-COF was slightly decreased, possibly due to the reduction of oligomers (Fig. 2b).

X-ray photoelectron spectroscopy (XPS) was employed to examine the detailed chemical states of elements in the catalysts before and after oxidation (Supplementary Figs. 14–17). In the overall XPS spectra, it can be observed that the O 1*s* characteristic peaks of O-LZU-190 and O-LZU-191 are significantly enhanced compared with those before oxidation, also indicating an increase in oxygen content (Supplementary Fig. 14). The O 1*s* fine spectrum reveals a distinct peak at a binding energy around 533.0 eV in both O-LZU-190 and O-LZU-191, which is attributed to the stretching vibration of C−OH bond[43]. However, no significant difference can be observed between O-BO-COF and BO-COF (Fig. 2c and Supplementary Fig. 15). Moreover, the proportion of C − OH in O-LZU-190 is higher than that in O-LZU-191, which corresponds to the greater abundance of oxidizable sites in LZU-190 (Fig. 2d). Furthermore, the solid state ^{13}C CP/MAS NMR spectra exhibit increased signals at around 150 ppm for both O-LZU-190 and O-LZU-191, indicating the formation of phenol group on the C6 carbon of benzoxazole ring after oxidation (Fig. 2e and Supplementary Figs. 18–19)[41,42,44]. Concurrently, the solid state ^{1}H MAS NMR spectra of LZU-190 showed considerably increased spinning sideband manifold after oxidation, as illustrated by the tripling of the 1H second moment M2, which is attributed to the enhanced 1H-1H homonuclear dipolar coupling among hydroxyl groups (likely between layers), and hence

https://doi.org/10.1038/s41467-025-59771-6

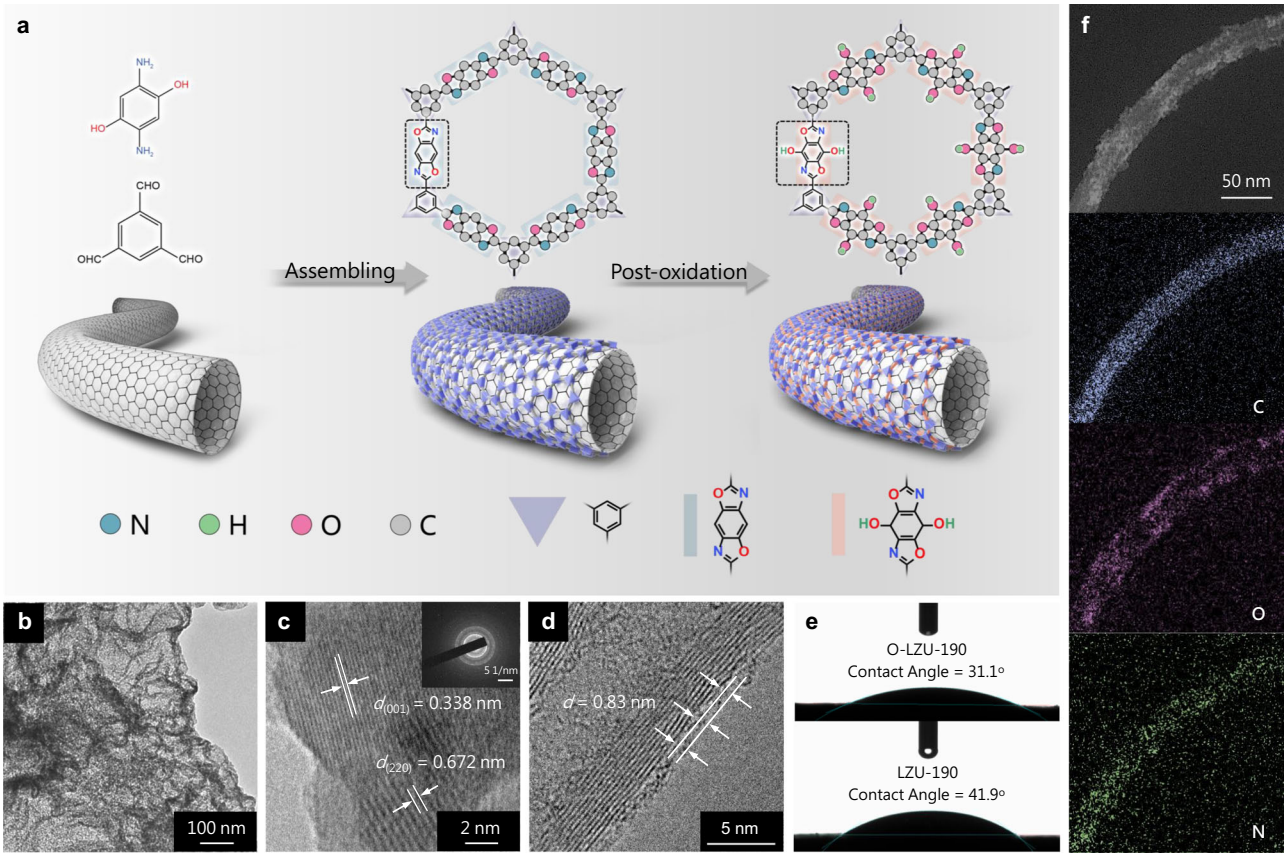

Fig. 1 | Synthesis and morphology characterizations. a Schematic illustration of O-LZU-190@CNT synthesis, CNT: carbon nanotube. **b** TEM and **c** HRTEM images of O-LZU-190 (inset: SAED pattern). **d** HRTEM image of O-LZU-190@CNT. **e** Images of static water-droplet contact for O-LZU-190 and LZU-190. **f** Elemental mappings of O-LZU-190@CNT.

also suggested the presence of increased phenol species resulting from oxidation (Fig. 2f and Supplementary Fig. 20)[45,46].

We also conducted near-edge X-ray absorption fine structure (NEXAFS) measurements to examine the electronic bonding within the catalysts. The O 1*s* NEXAFS spectra unveil distinct peaks at 532.3, 537.6, and 542.1 eV in O-LZU-190, which is ascribed to π* (C−OH), σ* (C−OH), and π* (C = O), respectively[47–49]. These chemical bonds originate from the hydroxyl and quinone groups generated through oxidation, corroborating the findings from XPS and NMR measurements (Fig. 2g). Moreover, the C *K*-edge NEXAFS profile of LZU-190 reveals four peaks at 284.7, 286.7, 288.0, and 292.9 eV, corresponding to π* (C−C), π* (C = C), π* (C−O−C/C−OH) and σ* (COF carbon backbone), respectively (Fig. 2h)[50,51]. Delightfully, the entire spectral features of O-LZU-190 exhibit a consistent shift towards higher energies, indicating an enhanced electronegativity of the carbon backbone after oxidation[52]. Furthermore, the intensity of the O-LZU-190 featured at 288.6 eV (π* of C−O−C/C−OH) exhibits a notable increase when compared with LZU-190, which also supports the formation of hydroxyl groups (Fig. 2h). This finding is further confirmed by the Fourier transform infrared (FT-IR) spectra, where discernible emerging signals of C−OH stretching vibrations are observable (Supplementary Fig. 21)[53,54].

Electrocatalytic activity evaluation

The evaluation of the electrocatalytic performances for OER was conducted using a three-electrode electrolytic cell with O_2-saturated 1.0 M KOH as electrolyte. Based on linear sweep voltammetry (LSV) tests using glassy carbon electrode (GCE), we observed that, aside from BO-COF(@CNT), other post-oxidation modified catalysts exhibited obviously enhanced OER activities (Fig. 3a). Thereinto, O-LZU-190@CNT requires 257.7 ± 0.6 mV to achieve a current density of 10 mA·cm^{-2} and possesses a small Tafel slope of 26.3 ± 0.7 mV·dec^{-1}, both of which are lower than those of other comparative catalysts and the benchmark RuO_2 (Fig. 3b and Supplementary Figs. 22–28). Notably, O-LZU-190@CNT displays a greater improvement in activity when compared with O-LZU-191@CNT, owing to its higher site density for oxidation. Whereas, the performance of the catalyst is not significantly improved by pyrolysis in N_2 atmosphere (Supplementary Fig. 29). Besides, LZU-190 and LZU-191 are expected to undergo marked activation during the OER process, potentially as a result of electro-oxidation (Supplementary Figs. 30–32). There is minimal variation in the electrochemical active surface area (ECSA) among the compared catalysts (Supplementary Figs. 33–36). Nevertheless, O-LZU-190@CNT exhibited fast charge-transfer kinetics with the smaller resistance compared to the other catalysts, while maintaining an almost 100% Faradaic efficiency (Supplementary Figs. 37–39). According to the Arrhenius plots (Supplementary Fig. 40), the apparent activation energy (E_a) of O-LZU-190@CNT is 46.9 ± 1.0 kJ·mol^{-1}, being significantly lower than that of LZU-190@CNT (112.4 ± 7.6 kJ·mol^{-1}). The relative turnover frequencies (TOFs) of the catalysts were determined based on electrical double-layer capacitor data obtained from cyclic voltammetry (CV) scans. Remarkably, the TOF of O-LZU-190@CNT reaches an impressive value of 23.0 ± 0.2 s^{-1} and 43.0 ± 1.6 s^{-1} at overpotentials of 280 mV and 300 mV, respectively, which represents a noticeable improvement of over 20 times compared with LZU-190@CNT. (Fig. 3c). It is worth noting that the intrinsic activity of O-LZU-190@CNT is one of the best among the reported metal-free electrocatalysts. (Tables S1).

We further evaluated the OER performance of O-LZU-190@CNT on various conductive substrates. All the self-supporting electrodes display good performances at ampere-level current density. Specifically, it requires overpotentials of 328.7 ± 5.8, 353.0 ± 1.0, 348.7 ± 5.8,

https://doi.org/10.1038/s41467-025-59771-6

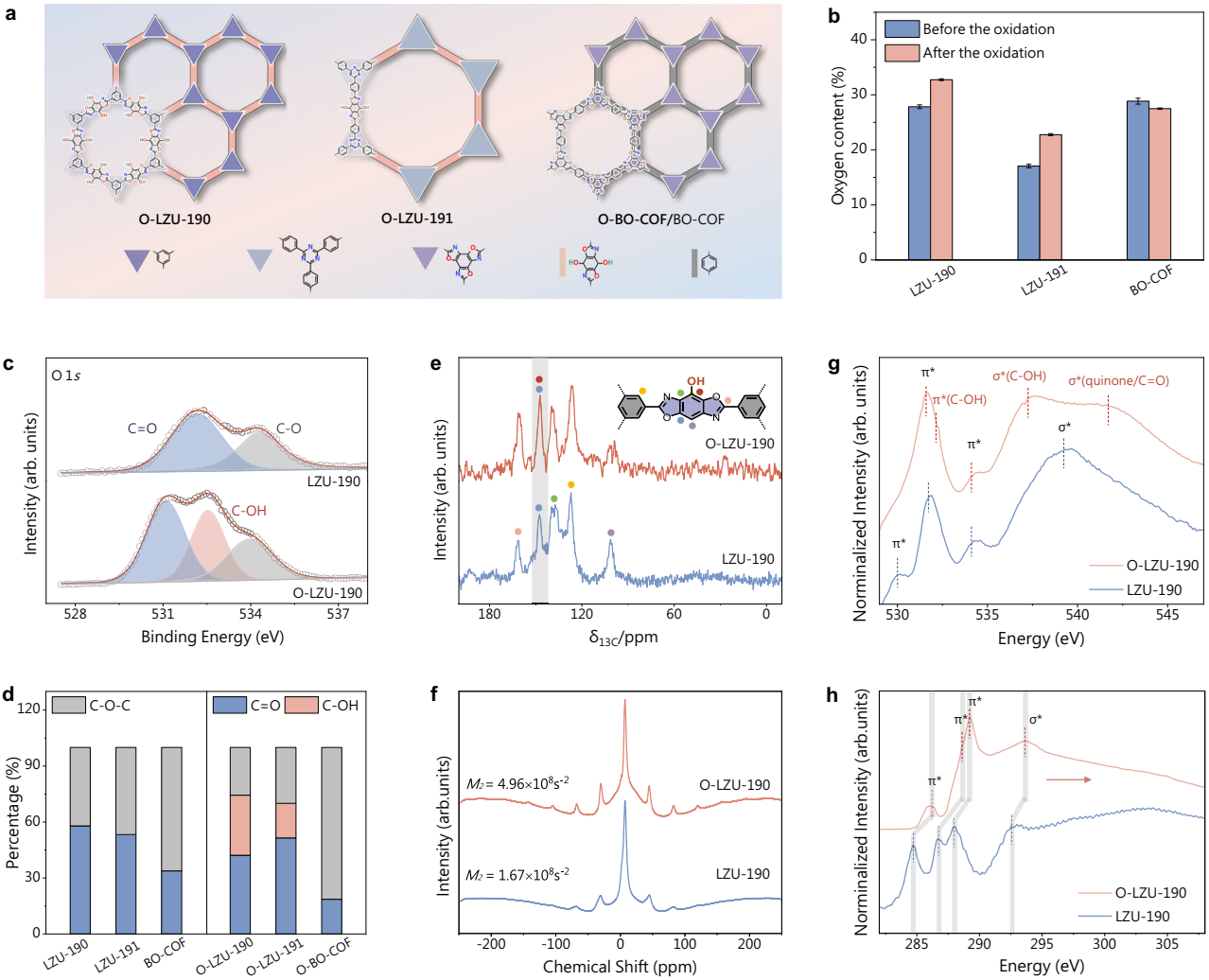

Fig. 2 | Structural analysis. a Structural models of O-LZU-190, O-LZU-191, and O-BO-COF. **b** The O contents of three COFs before and after oxidation. Error bars represent standard deviation, $n = 3$ independent replicates. **c** O 1*s* XPS spectra of LZU-190 before and after oxidation. **d** The XPS area ratio of O species in the three COFs before and after oxidation. **e** ^{13}C CP/MAS NMR spectra, **f** ^{1}H NMR spectra, **g** O *K*-edge NEXAFS profiles and **h** C *K*-edge NEXAFS profiles of LZU-190 and O-LZU-190. Source data are provided as a Source Data file.

380.7 ± 23.0, and 344.3 ± 12.1 mV to drive a current density of 1.0 A·cm^{-2} on Au foam (AuF), carbon cloth (CC), Co foam (CoF), Cu foam (CuF), Ni foam (NiF), and Ti mesh (TiM), respectively, being comparable to the advanced metal-based catalysts (Fig. 3d, Supplementary Fig. 41 and Table S2). Moreover, the performance of O-LZU-190@CNT is more advantageous than that of commercial RuO_2 with the increase of current density (Supplementary Fig. 42). Importantly, O-LZU-190@CNT exhibits notable stability, with negligible potential fluctuations observed during continuous chronoamperometry tests at various current densities ranging from 0.1 A·cm^{-2} to 1.0 A·cm^{-2}. Particularly, when operating at a high current density of 1.0 A·cm^{-2} for over 250 h, the potential fluctuations remain within 1.7 mV (Fig. 3g). Furthermore, the polarization curve retained with minimal alteration even after undergoing 100,000 CV cycles (Supplementary Fig. 43). By multiplying the current density by the lifetime/operating time, O-LZU-190@CNT demonstrates a total charge transfer over 8×10^5 C·cm^{-1}, while exhibiting a notably lower degradation rate of 0.1 mV·h^{-1} (Fig. 3h and Table S3). We further conducted a series of structural characterizations to investigate the structural stability of the studied catalysts after stability tests (Supplementary Figs. 44–46 and Table S4). The catalyst's structure was confirmed to remain stable after prolonged electrolysis by the results of PXRD and FT-IR. Moreover, ICP-MS analysis revealed negligible metal contents in various components and electrolytes before and after electrocatalysis (Supplementary Fig. 47 and Table S5). Additionally, control experiments using purified KOH electrolyte demonstrated no significant performance deviation from standard KOH in OER polarization measurements, effectively excluding any substantial interference from metal impurities in the catalytic system (Supplementary Fig. 48).

Interestingly, O-LZU-190@CNT also exhibits notable catalytic activity and stability in simulated seawater, likely benefiting from its pure covalently organic nature, which makes it insensitive to Cl^- corrosion. Firstly, the activity of O-LZU-190@CNT in simulated seawater is not much worse than that in 1.0 M KOH. Specifically, O-LZU-190@CNT exhibits an overpotential of 266.0 ± 1.0 mV at 10 mA·cm^{-2} (with a Tafel slope of 39.3 ± 3.2 mV dec^{-1}) on GCE in a solution of 1.0 M KOH + 0.5 M NaCl (Supplementary Fig. 49). Moreover, it requires an overpotential of 342.0 ± 2.0 mV to achieve a current density of 1.0 A·cm^{-2} on CC (with a Tafel slope of 64.3 ± 0.5 mV dec^{-1}), which is even 11 mV better than that in pure 1.0 M KOH. Additionally, the applied potential of O-LZU-190@CNT is only increased by 7.6% at a constant current density of 0.5 A·cm^{-2} after 30 h of stability test (Supplementary Fig. 50). These results indicate the sustained electrocatalytic properties of O-LZU-190@CNT.

https://doi.org/10.1038/s41467-025-59771-6

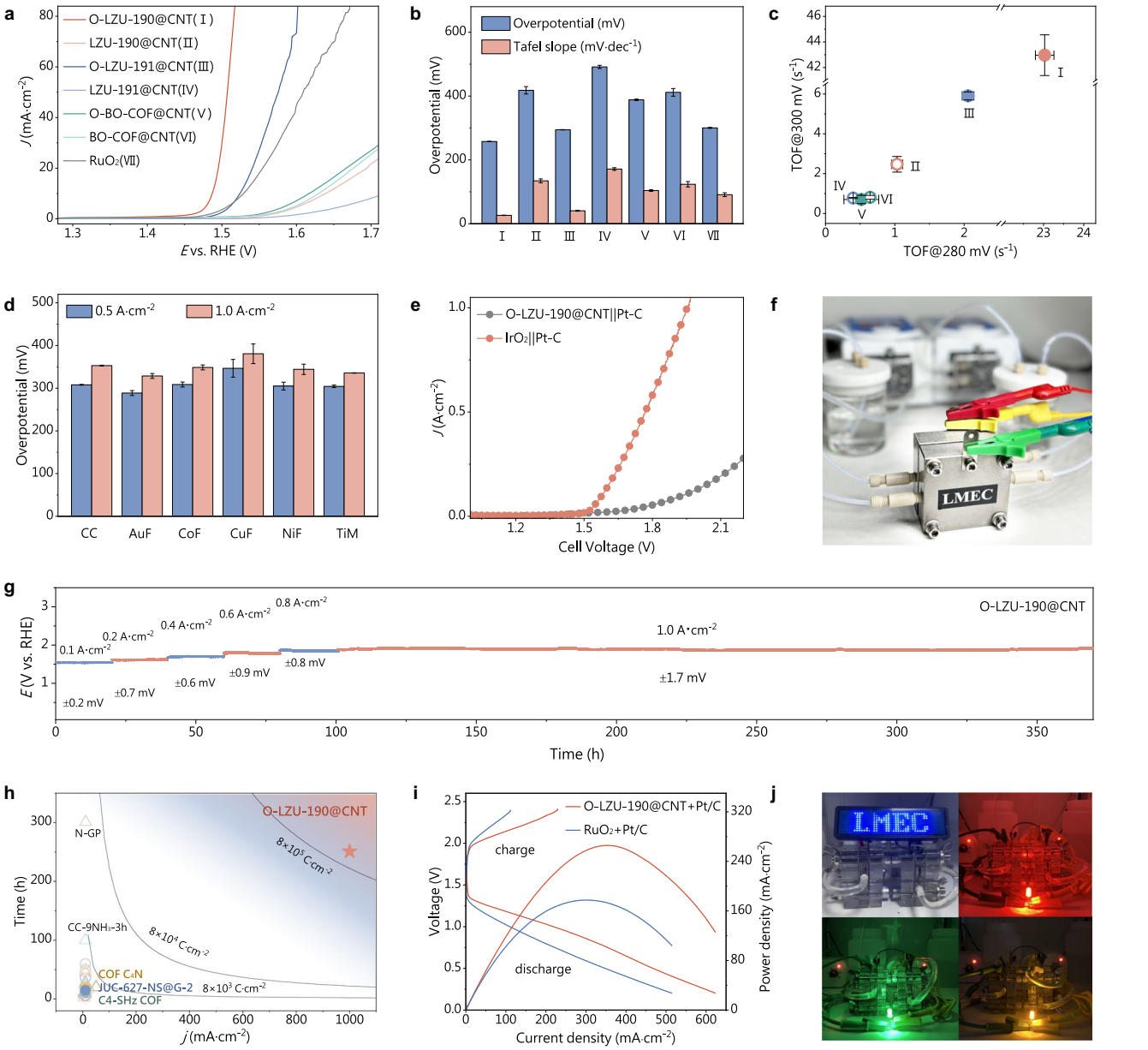

Fig. 3 | Electrocatalytic performances and device applications. a Polarization curves of catalysts on GCE in O_2-saturated 1 M KOH at a scan rate of 5 mV·s^{-1}. **b** Corresponding overpotentials at 10 mA·cm^{-2} and Tafel slopes of catalysts in **a**. **c** TOFs of catalysts at 280 mV and 300 mV. **d** Overpotentials of O-LZU-190@CNT at 0.5 A·cm^{-2} and 1.0 A·cm^{-2} on different conductive substrates. **e** The device activities of O-LZU-190@CNT and the benchmark commercial catalysts. **f** Photograph of the MEA electrolyzer device. **g** Multi-chronoamperometry tests of O-LZU-190@CNT, and the voltage fluctuations corresponding to each current density are calculated using variance and labeled. **h** Comparison of the total amount of charge transferred within lifetime/operation time with those reported metal-free catalysts. **i** The charge-discharge polarization curves of O-LZU-190@CNT+Pt/C and RuO_2 + Pt/C based zinc-air batteries. **j** Photographs of LED panel (LMEC represents *Lab of Molecule-based Energy Chemistry*) and colored lamps powered by two O-LZU-190@CNT+Pt/C based batteries. Error bars represent standard deviation, $n = 3$ independent replicates. Source data are provided as a Source Data file.

Given the impressive electrocatalytic performances of O-LZU-190@CNT, we evaluated its industrial application potential in both the membrane electrode assembly (MEA) electrolyzer device and zinc-air battery (ZAB) system[55]. The anion exchange membrane (AEM) electrolyzer, catalyzed by O-LZU-190@CNT||Pt/C proved capable of supporting a current density of 1.0 A·cm^{-2} at 1.95 V. In contrast, the IrO_2||Pt/C system could only attain one-tenth of that current density at the same cell voltage (Fig. 3e, f). Additionally, a two-electrode rechargeable ZAB, assembled with O-LZU-190@CNT and Pt/C as the OER and ORR electrocatalyst, respectively, demonstrates an open circuit potential of 1.44 V, which is higher than that of RuO_2+Pt/C (Supplementary Fig. 51). Furthermore, the O-LZU-190@CNT+Pt/C based ZAB also exhibits reduced charging and discharging potentials, along with higher power density, energy density, and specific capacity than those of RuO_2+Pt/C based ZAB (Fig. 3i and Supplementary Fig. 52). Besides, the O-LZU-190@CNT +Pt/C based ZAB demonstrates voltage stability across various current densities ranging from 2.0 to 20.0 mA·cm^{-2}, and maintains sustainable cyclic charge-discharge for a duration of 160 h (Supplementary Fig. 53). In addition, two series-wound of O-LZU-190@CNT+Pt/C based ZABs were capable of directly powering LED panel or lamps (Fig. 3j).

Insights into OER mechanism

To gain a comprehensive understanding of the OER mechanism, *Operando* attenuated-total-reflection surface enhanced infrared adsorption spectroscopy (ATR-SEIRAS) was employed to analyze the adsorption behaviors of surface reaction intermediates[56]. Notably, a distinct absorption peak at 1672 cm^{-1}, attributed to the C = O[57], intensified with an increase in applied potential, indicating deeply oxidation of the organic matrixes to form quinone groups during OER (Fig. 4a and Supplementary Fig. 54). Furthermore, CV tests also revealed a reversible proton-coupled electron transfer between the phenolic and quinone groups presented in O-LZU-190 during the electrochemical redox process (Fig. 4b)[58,59]. These findings demonstrated that quinone-modified benzobisoxazole should be the actual active sites for OER. Moreover, *operando* ATR-SEIRAS detected two distinct peaks at 1146.0 cm^{-1} and 1455.6 cm^{-1} as the potential increased (Fig. 4a and Supplementary Fig. 54). These peaks correspond to the O−O bond and linearly bonded superoxol species, both of which are crucial intermediates in the OPM-type OER[47,60]. To clarify whether the catalyst follows OPM or AEM before and after oxidation, *operando* differential electrochemical mass spectrometry (DEMS) was conducted with isotope labeling experiments. Typically, the presence of ^{16}O and ^{18}O adsorbates on active sites can produce $^{32}O_2$ and $^{36}O_2$ by coupling through OER via the OPM[61]. It is intriguing that O-LZU-190@CNT consistently generated $^{32}O_2$, $^{34}O_2$, and $^{36}O_2$ in each LSV cycle when $H_2{}^{18}O$ was used as the supporting solution, whereas LZU-190@CNT only produced $^{34}O_2$ and $^{36}O_2$ (Fig. 4c and Supplementary Fig. 55). In addition, the production of $^{36}O_2$ was still detectable when tested in the $H_2{}^{16}O$ electrolyte after ^{18}O was adsorbed on the surface of O-LZU-190@CNT by CV scans (Supplementary Fig. 56). Consequently, O-LZU-190@CNT satisfies the OPM pathway, whereas LZU-190@CNT fails to meet the criteria.

Utilizing density functional theory (DFT) calculations, we further explored possible reaction pathways and catalytic mechanisms of the catalysts before and after oxidation. Based on the experimental results mentioned, we proposed oxidized benzobisoxazole with quinone groups as the active unit of O-LZU-190. To investigate the most likely active site of the catalysts in their pre- and post-oxidation states, we conducted DFT calculations to compare the intermediate adsorption energies and the corresponding energy profiles on four kinds of positively charged C sites in the catalytic models. The results suggest that the active intermediates are preferentially adsorbed at different positions of the benzobisoxazole unit for AEM and OPM, respectively. Specifically, in the case of OPM, the C3 site appears more suitable for OER due to the appropriate distances of two adjacent oxygen species and its lowest OH adsorption energy in O-LZU-190 (Supplementary Fig. 57). For AEM, the lowest energy barrier was found at the C1 site in both LZU-190 and O-LZU-190 (Supplementary Figs. 58–61). Interestingly, when following the OPM, the interatomic O−O distance between adjacent O* on O-LZU-190 (2.615 Å) is much shorter than that on LZU-190 (3.218 Å), which might promote the coupling of O − O radicals (Fig. 4d). For LZU-190, the rate-determining step (RDS) for the OPM pathway is predicted to be the adsorption of OH* with an energy barrier of 2.121 eV, which is higher than the RDS of AEM pathway (TS for OOH* formation with an energy barrier of 1.955 eV). However, the energy barrier appears to be significantly reduced to 1.276 eV on the oxidation structure for OPM pathway, indicating that OH* might attach more easily to O-LZU-190. The RDS also shifts from OH* formation to TS of O−O coupling with an optimal energy barrier of merely 1.493 eV, which could align with its observed electrocatalytic performance. This barrier value is obviously lower than that of the RDS (1.779 eV) in AEM pathway (Supplementary Fig. 62). These calculations indicate that the OPM and AEM would be more favorable for O-LZU-190 and LZU-190, respectively, which is generally consistent with the findings from *operando* spectroscopy and DEMS with isotope labeling. Moreover, as the *OH intermediates are electrophiles that can be probed by nucleophiles, we employed the methanol oxidation reaction (MOR) to gain insight into the OH adsorption on the catalysts[62]. Obviously, the disparity between MOR and OER increases after oxidation, indicating that the adsorption of OH* on O-LZU-190@CNT is stronger than that on LZU-190@CNT (Fig. 4f). Additionally, the *p*-band center of the active C atom in O-LZU-190 (−7.16 eV) is slightly lower than that of LZU-190 (-6.93 eV), indicating a higher affinity of O-LZU-190 for adsorbing oxygen intermediates (Fig. 4g, h)[63]. Furthermore, we conducted molecular dynamic (MD) simulations in 1 M KOH solution and calculated the radial distribution function (RDF) of oxygen species relative to the benzobisoxazole center of catalysts. The RDF plot of O-LZU-190@CNT shows that O species are positioned somewhat closer to the benzobisoxazole center compared with that of LZU-190@CNT (Supplementary Figs. 63–65), which suggests that it is more hydrophilic after oxidation, being consistent with the contact angle measurements and the above analyzes. In short, the post-oxidation modification may enhance the adsorption of OH* on the benzobisoxazole unit of O-LZU-190 and potentially optimize the adsorption position of neighboring O* intermediates, thereby reducing the distance between oxygen radicals for facilitating their coupling. This could contribute to a shift in the OER pathway from AEM to OPM, thereby accelerating the OER kinetics.

In summary, we demonstrate that the adsorption of metal-free benzoxazole-based COFs for OH* intermediates in alkaline OER can be effectively enhanced by a post-oxidation strategy. This post-oxidative modification is also conducive to modulating the distance of adjacent O intermediates, which facilitates the direct coupling of O−O radicals and conforms to the oxide path mechanism (OPM). Therefore, the designed O-LZU-190@CNT electrocatalyst, owing to its switched OER pathway, exhibits enhanced activity and stability relative to conventional metal-free electrocatalysts. Specifically, it exhibits an OER overpotential of 257.7 ± 0.6 mV at 10 $mA{\cdot}cm^{-2}$, along with a small Tafel slope of 26.3 ± 0.7 $mV{\cdot}dec^{-1}$, while maintaining good durability during a 250 h operation at 1.0 $A{\cdot}cm^{-2}$. Our investigations not only offer evidence for the occurrence of OPM in all-organic electrocatalysts during OER, but also present cutting-edge perspectives and valuable guidance for the design of all-organic catalysts in sustainable industrial applications.

Methods

Material preparation

1,3,5-Tris-(4-formylphenyl) triazine (97%), 1,3,5-triamino-2,4,6-benzenetriol trihydrochloride (TABT, 97%) were purchased from *Shanghai Kaiyulin* pharmaceutical technology Co., Ltd. 2,5-Diamino-1,4-benzenediol dihydrochloride (97%), 1,3,5-triformylbenzene (96%), *N*, *N*-dimethylformamide (DMF, 99%), tetrahydrofuran (THF, AR, 99%), and MWCNTs-NH_2 (8-15 nm in diameter, ca. 50 μm in length) were obtained from *Aladdin*. Benzimidazole (96%), terephthaldehyde (TPA, 95%), Nafion 117 solution (~5% in a mixture of lower aliphatic alcohols and water), potassium hydroxide (KOH, semiconductor grade, 99.99%), potassium hydroxide (AR, 95%), mesitylene (98%, extra dry, with molecular sieves, water ≤ 50 ppm (by K.F.), Energyseal), and *N*-methyl pyrrolidone (NMP, 99%) were purchased from *Energy Chemical*. Dry CH_2Cl_2 (99.9%, water ≤ 50 ppm), 2,3-dichloro-5,6-dicyano-1,4-benzoquinone (DDQ, 98%) were purchased from *Innochem*. Carbon cloth (CC, WOS1009) was obtained from *Phychemi* Company. The carbon cloth was cut into the required size, washed several times with distilled water, ethanol and acetone, respectively, then soaked in a round-bottomed flask filled with concentrated nitric acid at a temperature of 100 °C with reflux for 2 h, washed with distilled water and anhydrous ethanol to neutrality to remove impurities and improve the hydrophilicity of the carbon

https://doi.org/10.1038/s41467-025-59771-6

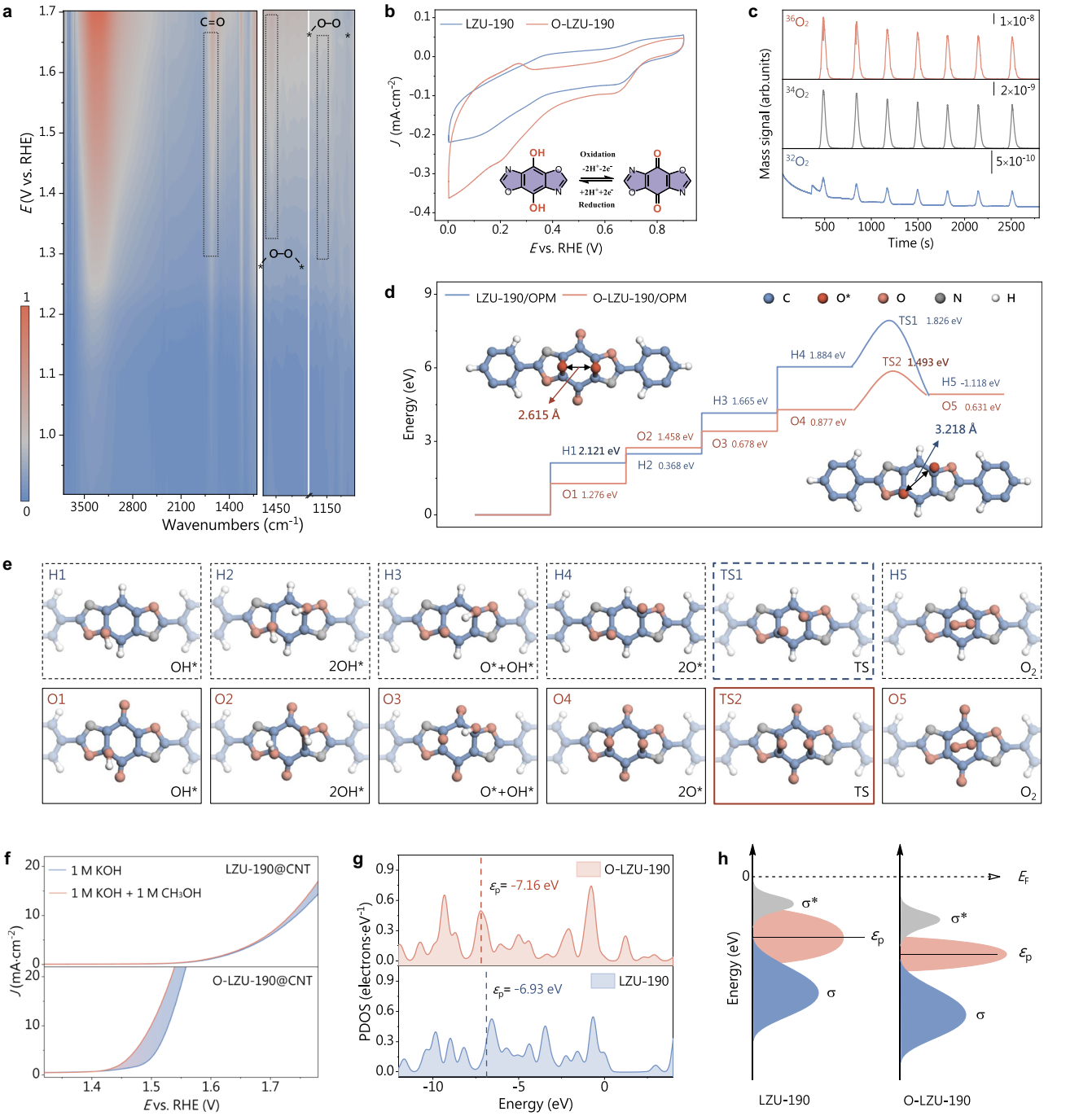

Fig. 4 | Exploring the OER mechanism. a Potential-dependent *Operando* ATR-SEIRAS of O-LZU-190. **b** CV scans of O-LZU-190 and LZU-190 after the activation (inset: structural transformation of O-LZU-190 during electrochemical processes). **c** DEMS signals of O_2 products for O-LZU-190@CNT using $H_2^{18}O$ as the electrolyte solvent during seven times of LSV in the potential range of 1.1–1.7 V versus RHE, with a 5 mV·s^{-1} scan rate. **d** Gibbs free energy diagrams of LZU-190 and O-LZU-190 for the OPM pathway. All states corresponding to each reaction step depicted in Fig. 4e (insets: the interatomic distances of O–O coupling in symmetric dual active sites of O-LZU-190 and LZU-190, respectively). **e** The optimized configurations of key intermediates and transition state (TS) for OPM on LZU-190 (H1–H5, and TS1) and O-LZU-190 (O1–O5, and TS2). TS stands for the transition state. Color codes: blue, C; gray, N; red, O; white, H. **f** LSV curves for O-LZU-190@CNT and LZU-190@CNT in 1 M KOH with (red lines) and without methanol (blue lines). Filled area shows the current difference caused by MOR. **g** PDOS of *p* orbital for C atoms in O-LZU-190 and LZU-190, ε_p: *p*-band center. **h** Schematic *p*-band diagrams of O-LZU-190 and LZU-190. The bonding and antibonding states after OH adsorption are indicated by σ and σ*, respectively. E_F: Fermi level. Source data are provided as a Source Data file.

cloth, and dried in a vacuum oven at 60 °C for 12 h. Nickel foam (NiF), cobalt foam (CoF), copper foam (CuF) and gold foam (AuF) were gained from *Jiangteng Electronics* Co., LTD. In addition, titanium mesh (TiM, 600) was purchased from *Hebei Kangwei Metal Products* Co., Ltd. All of the substrates were first ultrasonically cleaned with acetone and ethanol to remove any oil and impurities on surface, then immersed in a HCl solution (3 M), and finally dried in a vacuum oven after washed with ultra-pure water before use. Ultrapure water (resistivity ≥ 18 MΩ·cm, conductivity ≤ 0.1 μs·cm^{-1}, TOC ≤ 10 ppb) was obtained from an ultrapure water preparation machine (Dingji, Milli-Q, IQ7003). The above chemical reagents were used without further purification unless otherwise noted.

Material synthesis

Synthesis of LZU-190, LZU-191, LZU-190@CNT, and LZU-191@CNT. 2,5-Diamino-1,4-benzenediol dihydrochloride (0.107 g, 0.50 mmol), 1,3,5-triformylbenzene (0.054 g, 0.335 mmol), and benzimidazole (0.177 g, 1.50 mmol) were weighed into a Pyrex tube. After that, NMP (2.25 mL) and mesitylene (2.25 mL) were then added to the solid powder mixture. The reactants in the Pyrex tube were rapidly frozen in a liquid nitrogen bath and then placed in a high pressure parallel organic synthesis device (EYELA PPV-4431), which was vacuumed to negative pressure. Upon warming to room temperature, the reaction was set at 185 °C and left undisturbed for 5 days. After the reaction was completed, the solid substance was centrifuged, washed with acetone and THF, and dried at room temperature. And then, DMF was used as solvent to extract the residual monomers or oligomers through Soxhlet extraction for 2 days. Finally, the powder was washed with methanol, and freeze-dried to obtain the product of LZU-190. Similarly, LZU-191 can be synthesized by replacing one of the reactive monomers 1,3,5-triformylbenzene, with 1,3,5-tris-(4-formylphenyl) triazine. In addition, additional 60 mg MWCNTs-NH_2 was incorporated for the synthesis of LZU-190@CNT and LZU-191@CNT at the same synthesis procedure. For comparison, we also prepared LZU-190@CNT with different proportions of CNT. Specifically, 24 mg, 30 mg, 40 mg, 120 mg, and 240 mg of CNT were introduced into the similar reaction system, resulting in the formation of LZU-190@CNT(5:1), LZU-190@CNT(4:1), LZU-190@CNT(3:1), LZU-190@CNT(1:1), and LZU-190@CNT(1:2), respectively.

Synthesis of BO-COF, and BO-COF@CNT. TABT (0.168 g, 0.60 mmol) and TPA (0.122 g, 0.90 mmol) were placed in a Pyrex tube (50 mL). The tube was degassed and filled with argon, keeping the flow rate of the gas constant, methyl alcohol (4 mL), pyridine (0.177 mL, 2.1 mmol), 1,3,5-trimethylbenzene (4 mL) and deionized water (0.2 mL) were added. The reaction mixture was sonicated to form a homogenous dispersion and then flash frozen at 77 K. It was degassed through three freeze-pump-thaw cycles. The mixture was then heated at 120 °C for 3 days without disturbance. The product was isolated by filtration, washed with acetone, and finally dried at 80°C under vacuum overnight to get a light brown powder. Next, the powder (0.191 g, 0.30 mmol by imine, 1 equiv.) was dispersed in 10 mL dry CH_2Cl_2 to form a uniform suspension. A solution of DDQ (calculated according to the feed amount of TABT, 0.817 g, 3.60 mmol, 2 equiv.) in CH_2Cl_2 (80 mL) was slowly added dropwise at room temperature with stirring. Sequentially, the above reaction mixture was stirred at room temperature for an additional 3 days. After the reaction was completed, the product was obtained, washed with CH_2Cl_2 and THF by centrifugation, subjected to Soxhlet extraction with THF for 24 h, and dried at 80 °C under vacuum overnight to yield a reddish-brown powder of BO-COF. Besides, an extra 60 mg MWCNTs-NH_2 was added for the synthesis of BO-COF@CNT at the same synthesis procedure.

Synthesis of post-oxidation modified catalysts. 50 mg LZU-190, LZU-190@CNT, LZU-190@CNT(5:1, 4:1, 3:1, 1:1, 1:2), LZU-191, LZU-191@CNT, BO-COF, and BO-COF@CNT were pyrolyzed with a heating rate of 5 °C·min^{-1} to 360 °C for 60 minutes under air in a muffle furnace. The resulting products were labeled as O-LZU-190, O-LZU-190@CNT, O-LZU-190@CNT(5:1, 4:1, 3:1, 1:1, 1:2), O-LZU-191, O-LZU-191@CNT, O-BO-COF, and O-BO-COF@CNT, respectively. Furthermore, a control material, denoted as N-LZU-190, was synthesized through the same process by pyrolyzing LZU-190 under an N_2 atmosphere.

Material Characterizations

Powder X-ray diffraction (PXRD) patterns were collected on a Rigaku MiniFlex600 powder X-ray diffractometer (CuKα radiation), over a 2θ range of 3.0° to 50.0°, with a step size of 0.02° and 2 s per step. The morphology of catalysts was characterized by scanning electron microscope (SEM, Zeiss EVO 10) and transmission electron microscope (TEM, JEM2100F). The thickness of catalysts was investigated using an atomic force microscope (AFM, Bruker Dimension ICON), and AFM images were processed using Gwyddion software. X-ray photoelectron spectroscopy (XPS) data were collected on the Escalab 250Xi X-ray photo-electron spectrometer to analyze the surface composition of samples. Thermogravimetric (TG) analyzes were performed on TA Q50, with a flow of N_2 or dry air, by heating from room temperature to 600 °C at a rate of 10 °C·min^{-1}. Solid-state nuclear magnetic resonance (NMR) and Fourier transform Infrared (FT-IR) were recorded on a Bruker AM-400 NMR spectrometer and a Nicolet 6700 Flex (Thermo Fisher), respectively. *Operando* ATR-SEIRAS measurements were performed in 1.0 M KOH at potentials ranging from 1.1 to 1.7 V *vs.* reversible hydrogen electrode (RHE) using a Nicolet iS50 FT-IR (Thermo Fisher, Supplementary Fig. 66). The N_2 sorption isotherms at 77 K were measured on Micrometrics ASAP 2020 Plus HD 88, and before testing, the samples were degassed at 120 °C for 12 h under high vacuum to eliminate any guest molecules. The specific surface areas and pore size distributions of samples were calculated using the Brunauer-Emmet-Teller (BET) and the Barrett-Joyner-Halenda method, respectively. The data of X-ray absorption near edge structure (XANES) was recorded at beamline 20A1 of Taiwan Light Source (TLS) of National Synchrotron Radiation Research Center (NSRRC). Metal element contents potentially contributing to OER activity was quantified by digesting catalyst and electrode materials in boiling concentrated HNO_3 (65–68%, trace metal grade, Aladdin) followed by ICP-MS analysis (Agilent 7700). *Operando* differential electrochemical mass spectrometry (DEMS) with isotope labeling was conducted using an QAS 100 device (detection limit: 3×10^{-15} mbar, sensitivity: 5×10^{-4} A·$mbar^{-1}$, electron impact ionization), following a similar approach as recently reported by the Lee group[61]. The DEMS configuration integrates a high-vacuum mass spectrometer with an ambient-pressure electrochemical cell via a medium-vacuum interface, allowing real-time monitoring of gaseous products through pressure-driven sampling (Supplementary Fig. 66). The working electrode was prepared by magnetron sputtering of Au onto a porous PTFE membrane (Linglu, ≥50% porosity, ≤20 nm pore size), followed by catalyst deposition via drop-casting. The three-electrode system was completed with a Pt wire counter electrode and Ag/AgCl reference in Ar_2-saturated 1.0 M KOH electrolyte. For isotope labeling studies, 1 M KOH was prepared using $H_2{}^{18}O$ as the electrode. The catalysts underwent consecutive CV cycles within a potential range of 1.1–1.7 V versus RHE, at a scan rate of 5 mV·s^{-1}, while simultaneously recording the mass signals of the gaseous products: $^{32}O_2$, $^{34}O_2$, and $^{36}O_2$. After labeling the catalyst surface with ^{18}O, the catalysts were washed with $H_2{}^{16}O$ to eliminate any physically adhered $H_2{}^{18}O$ molecules. Then, the catalysts were tested in 1.0 M KOH ($H_2{}^{16}O$) electrolyte, monitoring the same gas products.

Electrochemical Measurements

All the electrochemical performances were evaluated on the electrochemical workstation (CHI760E A19012b) using the classic three-electrode system in O_2-saturated 1.0 M KOH electrolyte (Volume: 50 mL). The KOH electrolyte (pH 13.6 ± 0.2) was freshly prepared before each test by dissolving 5.6 g KOH (semiconductor grade, 99.99%) in ultrapure water to a final volume of 100 mL, then stored in a polyethylene bottle. Prior to the measurements, the electrolyte is saturated with oxygen for 1 h. A saturated Hg/HgO electrode and platinum plate were employed as the reference electrode and counter electrode. The Hg/HgO reference electrode was calibrated versus a saturated Ag/AgCl reference electrode (in saturated KCl) by monitoring the open-circuit potential in argon-purged 1.0 M KOH solution for at least 1 h. Glassy carbon electrode (GCE, 5 mm) or various conductive supports (CC, NiF, CoF, CuF, TiM, and AuF, 0.2 cm^2) are used as working electrodes, which are coated with electrocatalysts. To prepare the working electrode, 3 mg catalysts were dispersed into a mixture of 800 μL water/ethanol (5:3, *V*/*V*) and 50 μL of 5 wt% Nafion solution.

After ultrasonication for 60 min to form a uniform ink-like suspension, 10 μL and 30 μL of catalyst ink were dropped on the surface of GCE and various conductive supports, respectively. The samples were then allowed to air-dry completely at room temperature, resulting in final catalyst loadings of 0.18 mg·cm^{-2} (GCE) and 1.06 mg·cm^{-2} (conductive supports). The MEA electrolyzer utilized a Fumasep FAA-3-PK-130 membrane (2.0 × 2.0 cm, 130 μm thickness) that was pretreated by soaking in 1.0 M KOH solution for 24 h. A 1.0 M KOH + 0.5 M NaCl electrolyte configuration was employed to simulate seawater. We also prepared Fe-free KOH according to the method reported in the literature[64]. Briefly, 2 g of $Ni(NO_3)_2{\cdot}6H_2O$ (99.99%, trace metal grade, Sigma-Aldrich) was dissolved in 4 mL of ultrapure water in an acid-cleaned polypropylene tube. After adding 20 mL of 1 M KOH to precipitate $Ni(OH)_2$, the mixture was vortexed, centrifuged, and the supernatant discarded. The precipitate was washed three times with ultrapure water (20 mL) and 1 M KOH (2 mL). For final purification, 50 mL of 1 M KOH was added to the washed $Ni(OH)_2$, vigorously agitated for 10 min, and allowed to settle for 3 h. The purified KOH supernatant was collected after centrifugation and stored in an acid-cleaned polypropylene bottle. For the OER experiment, each electrode was activated by cyclic voltammetry (CV) until it reached a relatively stable state. Linear sweep voltammetry (LSV) was then carried out at a scanning rate of 5 mV·s^{-1} within the potential range of 1.0 to 1.8 V vs. RHE with 95% *iR* calibration. The potential was calibrated against the reversible hydrogen electrode (RHE) by the formula:

$$E_{RHE} = E + E_{Hg/HgO} + 0.0591 \times pH \tag{1}$$

The Tafel slope of the catalyst is calculated according to the formula shown below:

$$\eta = a + b \log i \tag{2}$$

Where η is the overpotential, a is Tafel constant, b is Tafel slope, and i is the current. At a constant voltage, electrochemical impedance spectroscopy (EIS) was conducted using an AC voltage with an amplitude of 5 mV amplitude in the frequency range of 0.01 to 10^5 Hz.

Faraday efficiency (FE) was calculated according to the following equation:

$$FE = \frac{I_{ring}}{\varepsilon \times I_{disk}} \tag{3}$$

Where I_{ring} is the current collected by the Pt ring electrode when the ring potential is 0.4 V versus RHE, I_{disk} is the constant applied current on the disk electrode, and ε is the oxygen collection coefficient of the device, which is approximately 0.37. The electrochemically active surface area (ECSA) for all electrocatalysts was obtained by the equation:

$$ECSA = \frac{C_{dl}}{C_s} \tag{4}$$

Where C_{dl} denotes the electrochemical double-layer capacitance measured in the non-Faraday potential region (1.0 ~ 1.1 V vs. RHE) at various scanning rates of 20, 40, 60, 80, 100 and 120 mV·s^{-1}. C_s is the specific capacitance of the sample with a smooth surface under the same test conditions, and the value of C_s was determined to be 0.04 mF·cm^{-2} based on the typical reported values. The apparent activation energy (E_a) for OER was determined using the Arrhenius formula:

$$\frac{d(\log j_0)}{d(1/T)} = -\frac{E_{a,app}}{2.303R} \tag{5}$$

In the formula, j_0 represents the exchange current density obtained from Tafel plot (calculated from polarization curves at 20, 35, 50 and 65 °C, respectively), and T refers to the Kelvin temperature. The relative Turn Over Frequency (TOF) of the catalysts was determined by the following equation:

$$TOF = \frac{J \times N_A}{n \times F \times \tau} \tag{6}$$

Where J is the measured current density value under a specific overpotential value, N_A is the Avogadro number (6.022×10^{23}), n is the electron transfer number ($n = 4$ for OER), F is the Faraday constant (96485 C • mol^{-1}), and τ is the number of active sites participating in the OER calculated using the following formula:

$$\tau = \frac{\text{area of the } C_{dl} \text{ curve}}{\text{scan rate} \times 1.601 \times 10^{-19}} \tag{7}$$

The electrochemical performance of Zn–air battery was conducted on the same electrochemical workstation and battery test system (LANDdt). A PTFE membrane (SM150, thickness: 0.2 ± 0.05 mm, air permeability: 100–150 mL·cm^{-2}·min^{-1}, porosity: 10–15%) served as the gas diffusion layer in the metal-air cell configuration. The air cathode was prepared by coating a mixture of Pt/C and O-LZU-190@CNT (in a molar ratio of 1:1) onto carbon paper. The anode consisted of a 1 mm thick Zn plate, and the electrolyte used was a 6 M KOH solution with a 0.2 M $Zn(AcO)_2$ aqueous solution. For comparison, a control group was assembled using RuO_2 instead of O-LZU-190@CNT to construct the reference Zn-air battery. All tests for the Zn-air battery were conducted in an air environment without oxygen intake. The effective geometric area of the air cathode was 1.0 cm^2, while the Zn anode had an area of 0.5 cm^2. The open-circuit voltage was measured using the Open Circuit Potential-Time method within the range of -2.0 V to 2.0 V. The specific capacity was estimated based on the amount of consumed zinc, and the energy density was calculated using the specific capacity and the average discharge voltage. In addition, a long-term galvanostatic test was performed at a current density of 2 mA·cm^{-2} for the charge and discharge processes.

The equation of specific capacity and energy density, as reported, is according to the Eqs. (8) and (9), respectively:

$$\text{Specific capacity} = \frac{i \times t}{m_{Zn}} \tag{8}$$

$$\text{Energy density} = \frac{i \times t \times \bar{u}}{m_{Zn}} \tag{9}$$

Where i is the current, t is the service hours, m_{Zn} represents the weight of consumed zinc, and $\bar{u}$ represents the average discharge voltage.

DFT Calculations

The DFT calculations for geometric optimization, energy relaxations and electronic properties were performed using Cambridge Sequential Total Energy Package (CASTEP) module in the Materials Studio software. The calculations were conducted by spin-polarized DFT with the plane wave pseudo-potential (PWP) method. The Generalized Gradient Approximation (GGA) and Perdew-Burke-Ernzerhof (PBE) functional were used to describe exchange-correlation energies. The Broyden-Fletcher-Goldfarb-Shanno (BFGS) algorithm was used for minimizing structures. The transition states were searched through performing a linear synchronous transit (LST), followed by repeated conjugate gradient minimizations and quadratic synchronous transit (QST) maximizations until a transition state was finally located. The kinetic energy cutoff of plane wave was set at 500 eV. The self-consistent field (SCF) tolerance was 1×10^{-6} eV·atom^{-1} and density mixing was used for electronic minimizer on geometry optimization. The convergence criteria for total energy, stress, forces, and atomic

displacement were 1×10^{-5} eV·atom^{-1}, 5×10^{-2} GPa, 3×10^{-2} eV·Å^{-1}, and 1×10^{-3} Å, respectively. The atomic coordinates of all optimized computational models are provided in Supplementary Data 1.

Data availability

All data generated or analyzed during this study are included in this published article and its Supplementary Information files. Source data are provided with this paper.

References

1. Quan, L., Jiang, H., Mei, G., Sun, Y. & You, B. Bifunctional electrocatalysts for overall and hybrid water splitting. *Chem. Rev.* **124**, 3694–3812 (2024).
2. Liu, C. et al. Oxygen evolution reaction over catalytic single-site Co in a well-defined brookite TiO_2 nanorod surface. *Nat. Catal.* **4**, 36–45 (2021).
3. Li, J. Oxygen evolution reaction in energy conversion and storage: design strategies under and beyond the energy scaling relationship. *Nano-Micro Lett.* **14**, 112 (2022).
4. Liang, C. W. et al. Unravelling the effects of active site density and energetics on the water oxidation activity of iridium oxides. *Nat. Catal.* **7**, 763–775 (2024).
5. Chen, F.-Y., Wu, Z.-Y., Adler, Z. & Wang, H. Stability challenges of electrocatalytic oxygen evolution reaction: from mechanistic understanding to reactor design. *Joule* **5**, 1704–1731 (2021).
6. Li, A. L. et al. Enhancing the stability of cobalt spinel oxide towards sustainable oxygen evolution in acid. *Nat. Catal.* **5**, 109–118 (2022).
7. Guo, B. et al. Recent advances of transition metal basic salts for electrocatalytic oxygen evolution reaction and overall water electrolysis. *Nano-Micro Lett.* **15**, 57 (2023).
8. Guo, T., Li, L. & Wang, Z. Recent development and future perspectives of amorphous transition metal-based electrocatalysts for oxygen evolution reaction. *Adv. Energy Mater.* **12**, 2200827 (2022).
9. Yu, M., Budiyanto, E. & Tüysüz, H. Principles of water electrolysis and recent progress in cobalt-, nickel-, and iron-based oxides for the oxygen evolution reaction. *Angew. Chem. Int. Ed.* **61**, e202103824 (2022).
10. Wang, Z. et al. Efficient potential-tuning strategy through p-type doping for designing cathodes with ultrahigh energy density. *Natl Sci. Rev.* **7**, 1768–1775 (2020).
11. Leitao, E. M., Jurca, T. & Manners, I. Catalysis in service of main group chemistry offers a versatile approach to p-block molecules and materials. *Nat. Chem.* **5**, 817–829 (2013).
12. Xie, X. et al. Oxygen evolution reaction in alkaline environment: material challenges and solutions. *Adv. Funct. Mater.* **32**, 2110036 (2022).
13. Xu, H. et al. Carbon-based bifunctional electrocatalysts for oxygen reduction and oxygen evolution reactions: optimization strategies and mechanistic analysis. *J. Energy Chem.* **71**, 234–265 (2022).
14. Hu, C., Paul, R., Dai, Q. & Dai, L. Carbon-based metal-free electrocatalysts: from oxygen reduction to multifunctional electrocatalysis. *Chem. Soc. Rev.* **50**, 11785–11843 (2021).
15. Yang, D.-H., Tao, Y., Ding, X. & Han, B. H. Porous organic polymers for electrocatalysis. *Chem. Soc. Rev.* **51**, 761–791 (2022).
16. Hu, C., Gao, Y., Zhao, L. & Dai, L. Carbon-based metal-free electrocatalysts: recent progress and forward looking. *Chem. Catal.* **2**, 2150–2156 (2022).
17. Hu, C. & Dai, L. Doping of carbon materials for metal-free electrocatalysis. *Adv. Mater.* **31**, 1804672 (2019).
18. Geng, K. et al. Covalent organic frameworks: design, synthesis, and functions. *Chem. Rev.* **120**, 8814–8933 (2020).
19. Feng, X., Ding, X. & Jiang, D. Covalent organic frameworks. *Chem. Soc. Rev.* **41**, 6010–6022 (2012).
20. Cui, X. et al. Engineering organic polymers as emerging sustainable materials for powerful electrocatalysts. *Chem. Soc. Rev.* **53**, 1447–1494 (2024).
21. Zhao, X. J., Pachfule, P. & Thomas, A. Covalent organic frameworks (COFs) for electrochemical applications. *Chem. Soc. Rev.* **50**, 6871–6913 (2021).
22. Li, J. et al. Bulk COFs and COF nanosheets for electrochemical energy storage and conversion. *Chem. Soc. Rev.* **49**, 3565–3604 (2020).
23. Liu, R. et al. Covalent organic frameworks: an ideal platform for designing ordered materials and advanced applications. *Chem. Soc. Rev.* **50**, 120–242 (2021).
24. Cui, X. et al. Pyrolysis-free covalent organic framework-based materials for efficient oxygen electrocatalysis. *J. Mater. Chem. A* **9**, 20985–21004 (2021).
25. Liu, C. et al. One-dimensional van der Waals heterostructures as efficient metal-free oxygen electrocatalysts. *ACS Nano* **15**, 3309–3319 (2021).
26. Yang, C. et al. Theory-driven design and targeting synthesis of a highly-conjugated basal-plane 2D covalent organic framework for metal-free electrocatalytic OER. *ACS Energy Lett.* **4**, 2251–2258 (2019).
27. Mondal, S. et al. A thiadiazole-based covalent organic framework: a metal-free electrocatalyst toward oxygen evolution reaction. *ACS Catal.* **10**, 5623–5630 (2020).
28. Wang, R. et al. Exploring metal-free ionic covalent organic framework nanosheets as efficient OER electrocatalysts via cationic-π interactions. *Chem. Eng. J.* **478**, 147403 (2023).
29. Shi, Z. et al. Confined Ir single sites with triggered lattice oxygen redox: Toward boosted and sustained water oxidation catalysis. *Joule* **5**, 2164–2176 (2021).
30. Wang, Y. H. et al. Oxygen defect engineering promotes synergy between adsorbate evolution and single lattice oxygen mechanisms of OER in transition metal-based (oxy)hydroxide. *Adv. Sci.* **10**, 2303321 (2023).
31. Wang, C. et al. Identification of the origin for reconstructed active sites on oxyhydroxide for oxygen evolution reaction. *Adv. Mater.* **35**, 2209307 (2023).
32. Wu, J. X. et al. Atomically dispersed dual-metal sites showing unique reactivity and dynamism for electrocatalysis. *Nano-Micro Lett.* **15**, 120 (2023).
33. Righi, G. et al. On the origin of multihole oxygen evolution in haematite photoanodes. *Nat. Catal.* **5**, 888–899 (2022).
34. Wang, Y. et al. Unraveling oxygen vacancy site mechanism of Rh-doped RuO_2 catalyst for long-lasting acidic water oxidation. *Nat. Commun.* **14**, 1412 (2023).
35. Ding, H., Liu, H., Chu, W., Wu, C. & Xie, Y. Structural transformation of heterogeneous materials for electrocatalytic oxygen evolution reaction. *Chem. Rev.* **121**, 13174–13212 (2021).
36. Eum, D. et al. Coupling structural evolution and oxygen-redox electrochemistry in layered transition metal oxides. *Nat. Mater.* **21**, 664–672 (2022).
37. Jiang, Y. et al. Recent achievements in selenium-based transition metal electrocatalysts for pH-universal water splitting. *Nano Res* **17**, 5763–5785 (2024).
38. Zhang, T. et al. Spatial configuration of Fe–Co dual-sites boosting catalytic intermediates coupling toward oxygen evolution reaction. *Proc. Natl Acad. Sci.* **121**, e2317247121 (2024).
39. Chang, J. et al. Oxygen radical coupling on short-range ordered ru atom arrays enables exceptional activity and stability for acidic water oxidation. *J. Am. Chem. Soc.* **146**, 12958–12968 (2024).
40. Wang, N. et al. Doping shortens the metal/metal distance and promotes oh coverage in non-noble acidic oxygen evolution reaction catalysts. *J. Am. Chem. Soc.* **145**, 7829–7836 (2023).

41. Wei, P. F. et al. Benzoxazole-linked ultrastable covalent organic frameworks for photocatalysis. *J. Am. Chem. Soc.* **140**, 4623–4631 (2018).
42. Seo, J. M., Noh, H. J., Jeong, H. Y. & Baek, J. B. Converting unstable imine-linked network into stable aromatic benzoxazole-linked one via post-oxidative cyclization. *J. Am. Chem. Soc.* **141**, 11786–11790 (2019).
43. Lei, C. et al. High-performance metal-free nanosheets array electrocatalyst for oxygen evolution reaction in acid. *Adv. Funct. Mater.* **30**, 2003000 (2020).
44. Li, Y. et al. Laminated self-standing covalent organic framework membrane with uniformly distributed subnanopores for ionic and molecular sieving. *Nat. Commun.* **11**, 599 (2020).
45. Le Marchand, T. et al. ^{1}H-Detected biomolecular NMR under fast magic-angle spinning. *Chem. Rev.* **122**, 9943–10018 (2022).
46. Reif, B., Ashbrook, S. E., Emsley, L. & Hong, M. Solid-state NMR spectroscopy. *Nat. Rev. Methods Prim.* **1**, 2 (2021).
47. Liu, L. X. et al. Spectroscopic identification of active sites of oxygen-doped carbon for selective oxygen reduction to hydrogen peroxide. *Angew. Chem. Int. Ed.* **62**, e202303525 (2023).
48. Liu, L. et al. Atomically dispersed asymmetric cobalt electrocatalyst for efficient hydrogen peroxide production in neutral media. *Nat. Commun.* **15**, 4079 (2024).
49. Chen, S. et al. Chemical identification of catalytically active sites on oxygen-doped carbon nanosheet to decipher the high activity for electro-synthesis hydrogen peroxide. *Angew. Chem. Int. Ed.* **60**, 16607–16614 (2021).
50. Pei, Z. X. et al. A polymeric hydrogel electrocatalyst for direct water oxidation. *Nat. Commun.* **14**, 818 (2023).
51. Lu, S. et al. Dissolution of the heteroatom dopants and formation of ortho-quinone moieties in the doped carbon materials during water electrooxidation. *J. Am. Chem. Soc.* **144**, 3250–3258 (2022).
52. Ade, H. & Stoll, H. Near-edge X-ray absorption fine-structure microscopy of organic and magnetic materials. *Nat. Mater.* **8**, 281–290 (2009).
53. Liu, W. et al. Atomically-ordered active sites in NiMo intermetallic compound toward low-pressure hydrodeoxygenation of furfural. *Appl. Catal. B: Environ.* **282**, 119569 (2021).
54. Park, S. et al. Graphene oxide papers modified by divalent ions—enhancing mechanical properties via chemical cross-linking. *ACS Nano* **2**, 572–578 (2008).
55. Zheng, X. et al. Ru–Co pair sites catalyst boosts the energetics for the oxygen evolution reaction. *Angew. Chem. Int. Ed.* **61**, e202205946 (2022).
56. Zhao, Y. et al. Oxygen evolution/reduction reaction catalysts: from in situ monitoring and reaction mechanisms to rational design. *Chem. Rev.* **123**, 6257–6358 (2023).
57. Lu, S. et al. Phenanthrenequinone-like moiety functionalized carbon for electrocatalytic acidic oxygen evolution. *Chem* **8**, 1415–1426 (2022).
58. Lin, Y. M. et al. Electrocatalytic water oxidation at quinone-on-carbon: a model system study. *J. Am. Chem. Soc.* **140**, 14717–14724 (2018).
59. Lin, W. et al. Decoupled artificial photosynthesis via a catalysis-redox coupled COF||$BiVO_4$ photoelectrochemical device. *J. Am. Chem. Soc.* **145**, 18141–18147 (2023).
60. Liu, H. et al. Eliminating over-oxidation of ruthenium oxides by niobium for highly stable electrocatalytic oxygen evolution in acidic media. *Joule* **7**, 558–573 (2023).
61. Lin, C. et al. In-situ reconstructed Ru atom array on α-MnO_2 with enhanced performance for acidic water oxidation. *Nat. Catal.* **4**, 1012–1023 (2021).
62. Tao, H. B. et al. A general method to probe oxygen evolution intermediates at operating conditions. *Joule* **3**, 1498–1509 (2019).
63. Zhou, S. et al. Low-dimensional non-metal catalysts: principles for regulating p-orbital-dominated reactivity. *npj Comput. Mater.* **7**, 186 (2021).
64. Trotochaud, L., Young, S. L., Ranney, J. K. & Boettcher, S. W. Nickel–iron oxyhydroxide oxygen-evolution electrocatalysts: the role of intentional and incidental iron incorporation. *J. Am. Chem. Soc.* **136**, 6744–6753 (2014).

Acknowledgements

This work was supported by the National Natural Science Foundation of China (Nos. 22375079 and 22161021, C.T. H.; No. 22465019, J. Z.; No. 21890380, X.M. C.) and the project supported by Jiangxi Province Natural Science Foundation (Nos. 20224ACB214001 and 20242BAB26033, C.T. H.; No. 20232BAB203032, J. Z.). C.-T. H. acknowledges the support of Jiangxi provincial government (0224/09039001, C.T. H.).

Author contributions

C.T.H. conceived the idea, designed the study, and guided the project. L.H.Y. and J.Z. performed the experiments and most of the data analysis. H.M. L. and Q. W. performed solid state CP/MAS NMR measurements. Z.M. Y. performed the PXRD refinements. L.D. W. and Z.W. L. conducted catalytic performance tests on the ZAB system. X.F. Z. carried out sorption measurements. C.T.H. and X.F.Z. conducted theoretical calculations. H.M.L., M.Q.H., H.G.D., J.Y., and H.H.H. joined the discussion of data and gave useful suggestions. C.T.H., J.Z., and X.M.C. drafted the manuscript. All authors discussed and commented on the manuscript.

Competing interests

The authors declare no competing interests.

Additional information

Supplementary information The online version contains supplementary material available at https://doi.org/10.1038/s41467-025-59771-6.

Correspondence and requests for materials should be addressed to Chun-Ting He or Jia Zhang.

Peer review information *Nature Communications* thanks Junkuo Gao and the other anonymous reviewer(s) for their contribution to the peer review of this work. A peer review file is available.